Journal of Materials Chemistry A

An aluminum hydroxide-mediated synthesis of mesoporous metal oxides by mechanochemical nanocasting strategy

Journal:	*Journal of Materials Chemistry A*
Manuscript ID	TA-ART-06-2019-006727.R1
Article Type:	Paper
Date Submitted by the Author:	19-Sep-2019
Complete List of Authors:	Liu, Jixing; University of Tennessee Cheng, Huifang; Hebei University of Engineering Bao, Jiafeng; Shanghai Jiao Tong University Zhang, Pengfei; Shanghai Jiao Tong University, Department of Chemical Engineering; Oak Ridge National Laboratory, Liu, Miaomiao; University of Tennessee Leng, yan; University of Tennessee Zhang, Zihao; University of Tennessee Tao, Runming; University of Tennessee Liu, Jian; China Petroleum University, State Key Laboratory of Heavy Oil Zhao, Zhen; China University of Petroleum, State Key Lab of Heavy Oil Dai, Sheng; Oak Ridge National Laboratory,

An aluminum hydroxide-mediated synthesis of mesoporous metal oxides by mechanochemical nanocasting strategy

Jixing Liu[a,b,c], Huifang Cheng[d], Jiafeng Bao,[e] Pengfei Zhang[e,*], Miaomiao Liu[b,c], Yan Leng[b,c], Zihao Zhang[b,c], Runming Tao[b,c], Jian Liu[a,*], Zhen Zhao[a], Sheng Dai[b,c,*]

[a]State Key Laboratory of Heavy Oil and Beijing Key Lab of Oil & Gas Pollution Control, China University of Petroleum, Beijing 102249, P. R. China;

[b]Department of Chemistry, University of Tennessee–Knoxville, Tennessee 37996, United States

[c]Oak Ridge National Laboratory, Oak Ridge, Tennessee 37831, United States;

[d]College of Material Science and Engineering, Hebei University of Engineering, Handan 056038, Hebei, People's Republic of China;

[e]School of Chemistry and Chemical Engineering, Shanghai Jiao Tong University, Shanghai 200240, P. R. China

*Corresponding authors: P. F. Z. (E-mail: chemistryzpf@sjtu.edu.cn), J. L. (E-mail: liujian@cup.edu.cn), and S. D. (E-mail: dais@ornl.gov)

Abstract:

Mesoporous metal oxides (MOs) have attracted significant interest in heterogeneous catalysis due to their wide pore size and high pore volume. Herein, we present a facile mechanochemical nanocasting strategy featured by aluminum hydroxide as the mesoporous structure-directing agent, which surmounts the drawbacks associated with the wet template-assisted methods. In this procedure, by simply grinding the mixture of commercial aluminum hydroxide and MO precursors, a series of mesoporous MOs with high specific surface area and narrow pore size have been constructed in a short time (e.g., Fe_2O_3, 280 $m^2 \cdot g^{-1}$; Co_3O_4, 155 $m^2 \cdot g^{-1}$; CeO_2, 192 $m^2 \cdot g^{-1}$; ZrO_2, 170 $m^2 \cdot g^{-1}$; CuO_x-CeO_y, 177 $m^2 \cdot g^{-1}$; FeO_x-CeO_y, 170 $m^2 \cdot g^{-1}$; CoO_x-CuO_y-CeO_z, 154 $m^2 \cdot g^{-1}$; CoO_x-FeO_y-CeO_z, 133 $m^2 \cdot g^{-1}$). It is expected that this strategy may open up new opportunities for fabricating a number of advanced porous materials with abundant porosity in the near future.

1. Introduction

Mesoporous metal oxides (MOs) with high specific surface areas and narrow pore size distributions have drawn ever-increasing attention in recent years in numerous fields such as catalysis, energy storage, biomedicines, gas sensor, and so forth.[1-8] Those oxides are generally constructed by template-assisted methods, for instance self-template,[9–12] soft- or hard-templating methods.[13-17] For the self-template method, featured by metal-organic frameworks (MOFs), organic-inorganic hybrids, and hydroxides as precursors, is regarded an effective protocol to synthesize MOs with hollow and spheric architectures. Although great advances have achieved by this strategy, this method is known as wet and time-consuming processes.[18–20] In case of the soft-templating method, assisted by the self-assembly behavior of metal salts with Pluronic (P123 or F127), tailor-made (PEO-b-polystyrene, poly(methyl methacrylate), poly(vinylpyridine)-based copolymers), and non-Pluronic amphiphilic block copolymers, ordered organic-inorganic mesophases was introduced after organic template was removed. However, it has been well recognized that the application of this approach suffers from some limitations, for example, the mesostructure ordering of MOs constructed by this method is highly rely on the metal-oxide sources, solvents, co-solvents, coordinating agents, and experimental conditions (humidity, dip-coating speed, solvent evaporation speed, and calcination program). Moreover, this technology is complicated and costly, all of which greatly restrict its widespread application in the construction of mesoporous MOs.[14,21–24]

Toward this end, the hard-templating method is a more straightforward and general route to synthesize crystalline porous MOs.[25,26] This approach relies on the usage of polymer, mesoporous carbon, or mesoporous silica as templates to obtain desired mesoporous structure, and subsequent removal of the hard templates by calcination or etching to finally obtain mesoporous MOs. For this procedure, the porous solid template is firstly stuffed with MO precursors by coprecipitation or impregnation processes, and then to make MOs crystallize around the porous templates via calcinating the hybrid. Finally, the removal of template could incorporate abundant nanopores into crystalline MOs. Nonetheless, great progresses have been witnessed. Nevertheless, to date, this technology encounters some bottlenecks, for instance, the mesoporous characteristics of the final

porous oxides are absolutely dependent on the framework of the hard templates used. What's more, this procedure is still a wet process, which strongly requires metal salts to be soluble in solvents. In other words, these insoluble and refractory metal precursors cannot be employed in this technology, limiting the scope of MO precursors. Furthermore, this route is a laborious and time-consuming procedure, which requires a slow solvent evaporation and multiple impregnation processes to well cast the template.[27-30] Hence, the development of an alternative route that could overwhelm these defects of wet procedure is highly desirable for the synthesis of mesoporous MOs.

In this contribution, we present a novel and facile mechanochemical nanocasting strategy by using aluminum hydroxide as the mesoporous structure-directing agent. In this procedure, by simply grinding the mixture of aluminum hydroxide and MO precursors, a series of mesoporous MOs (e.g., Fe_2O_3, Co_3O_4, CeO_2, ZrO_2, CuO, CuO_x-CeO_y, FeO_x-CeO_y, CoO_x-CuO_y-CeO_z, and CoO_x-FeO_y-CeO_z) with relative high specific surface area and narrow pore size have been prepared. This finding opens a new strategy for the construction of mesoporous MOs, which is of great importance for the practical application.

2. Experimental

Synthesis of Mesoporous MOs by Ball Milling: All the mesoporous MOs were synthesized by the aluminium hydroxide-directing mechanochemical nanocasting strategy. Typically, 1.00 g MO precursor and x g (x = 0.500−2.00 g) aluminium hydroxide (CAS: 21645-51-2) were introduced to a commercially 25 mL zirconia reactor along with four zirconia ball bearings (total mass 8.6 g; diameter 2×1.0 cm, diameter 2×0.6 cm). The reactor was placed in a high-speed vibrating ball miller (Retsch MM400, Germany) and the mixtures were ball milled for 1 h at a vibrational frequency of 30 Hz. The resulting gel-like mixtures were calcinated at a desired temperature (heating rate: 2 °C·min^{-1}) in air. The obtained products were further treated in 1 M NaOH solution for 12 h at 60 °C, and then washed with deionized H_2O (repeating the process three times to remove the alumina template), followed by drying at 100 °C for 12 h. All the as-prepared crystalline oxides by aluminium hydroxide as structure-directing agent is denoted as MO-Y-Z (Y is mass ratio of aluminium hydroxide versus MO precursors, Z is calcination temperature). The reference samples synthesized

without template but the same procedure are named as MO-Z.

Preparation of FeO_x-CeO_y and CuO_x-CeO_y by Ball Milling: In a typical process, 0.350 g $Fe(NO_3)_3 \cdot 9H_2O$ (CAS: 7782-61-8), 1.00 g $Ce(NO_3)_3 \cdot 6H_2O$ (CAS: 10294-41-4) and 1.00 g aluminium hydroxide (CAS: 21645-51-2) were added into a commercially 25 mL zirconia reactor along with four zirconia ball and ball milled for 1 h at a vibrational frequency of 30 Hz. The resulting gel-like mixtures were calcinated at 400 °C (heating rate: 2 $^oC \cdot min^{-1}$) in air for 3 h. The obtained products were further treated in 1 M NaOH solution for 12 h at 60 °C, and then washed with deionized H_2O followed by drying at 100 °C for 12 h to obtain desired crystalline oxide phase. CuO_x-CeO_y was synthesized by the similar process as FeO_x-CeO_y, and the employed Cu source is $Cu(NO_3)_2 \cdot 4H_2O$ (CAS: 10031-43-3).

Preparation of CoO_x-FeO_y-CeO_z and CoO_x-CuO_y-CeO_z by Ball Milling: The synthesis process of CoO_x-FeO_y-CeO_z is completely identically to the mesoporous MOs mentioned above. 1.00 g $Ce(NO_3)_3 \cdot 6H_2O$ (CAS: 10294-41-4), 0.350 g $Fe(NO_3)_3 \cdot 9H_2O$ (CAS: 7782-61-8), 0.100 g $Co(NO_3)_2 \cdot 6H_2O$ (CAS: 10026-22-9), and 1.00 g aluminium hydroxide (CAS: 21645-51-2) were mixed and ball milled in a commercially 25 mL zirconia reactor along with four zirconia ball for 1 h at a vibrational frequency of 30 Hz. The desired crystalline oxide was obtained after being calcinated, NaOH treatment, washing, and drying at 100 °C for 12 h.

Electronic supplementary information (ESI) available: Characterization of the Catalysts, Catalytic CO Oxidation experiments, XRD patterns and N_2 adsorption-desorption isotherms for Fe_2O_3-Y-400, Fe_2O_3-Z and Co_3O_4-Z, and H_2-TPR profiles of Co_3O_4-1-400, Fe_2O_3-1-400, CeO_2-1-400, FeO_x-CeO_y-400, and CoO_x-FeO_y-CeO_z-1-400 catalysts.

3. Results and discussion

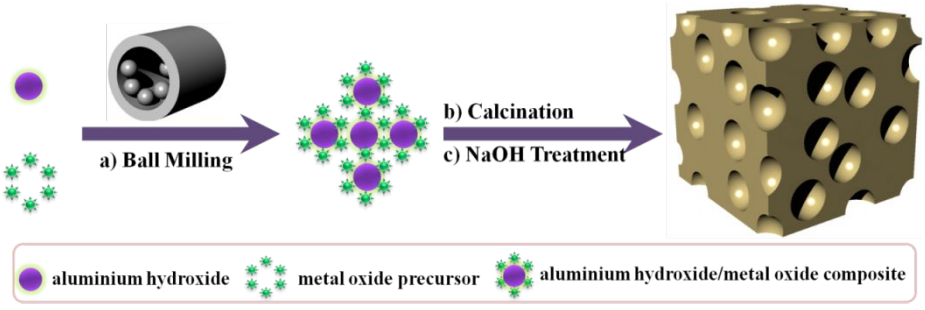

Scheme 1 Illustration of aluminum hydroxide-directing mechanochemical nanocasting towards the synthesis of mesoporous MOs.

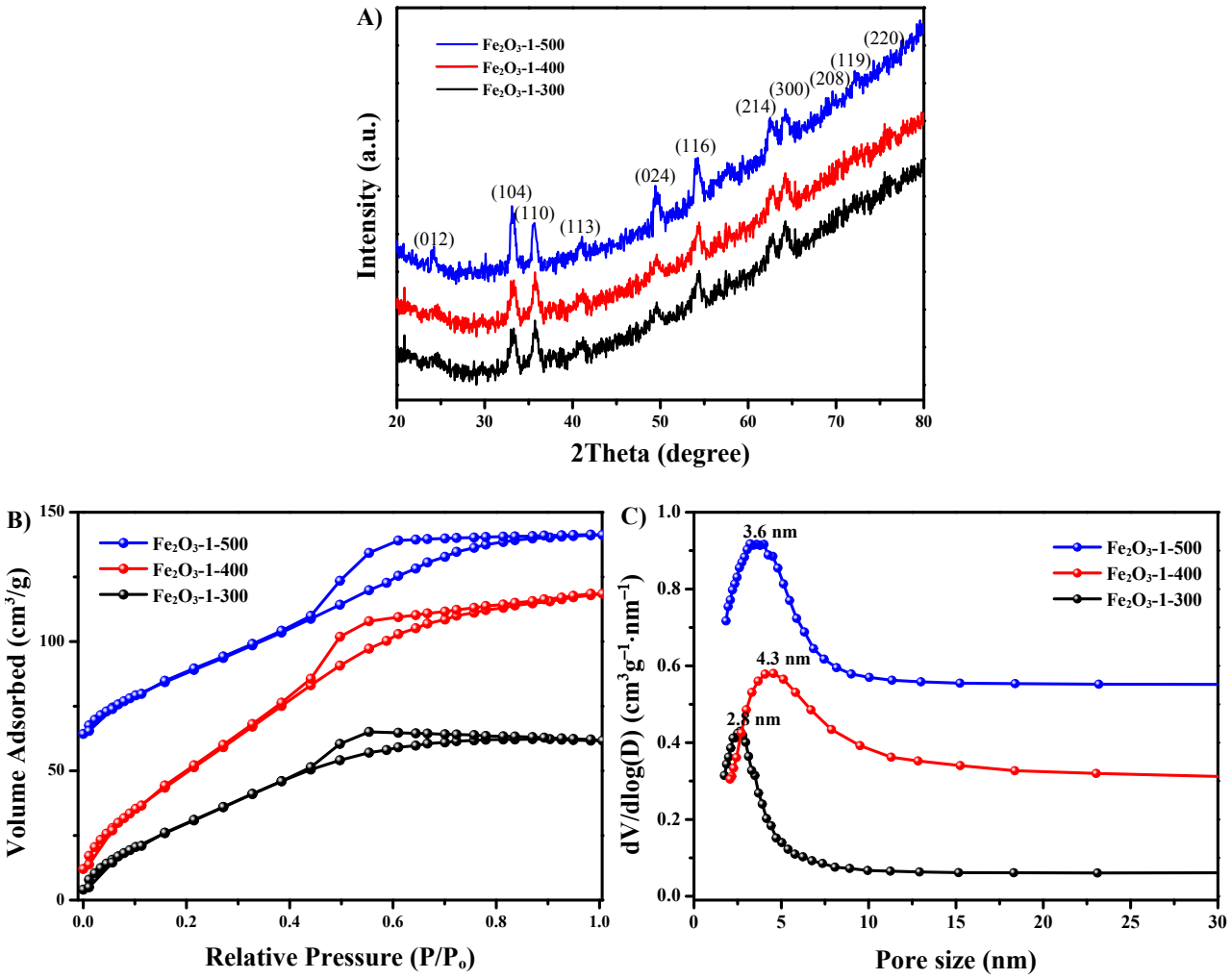

Figure 1. (A) XRD patterns, (B) N_2 adsorption-desorption isotherms (−196 °C), and the pore size distributions (C) of Fe_2O_3 prepared by mechanochemical nanocasting at different calcination temperatures.

In this study, a series of mesoporous MOs (e.g., Fe_2O_3, Co_3O_4, CeO_2, ZrO_2, CuO, CuO_x-CeO_y, FeO_x-CeO_y, CoO_x-CuO_y-CeO_z, and CoO_x-FeO_y-CeO_z) with relative high specific surface area and narrow pore size were successfully prepared by a facile mechanochemical nanocasting strategy, which uses aluminum hydroxide as the mesoporous structure-directing agent (as shown in **Scheme 1**). In this procedure, the MO precursors and aluminum hydroxide might form the highly uniform distribution of Al and metal (M) cationic oxides driven by the mechanical force and friction heating. After removal of Al from the as-formed MO framework, a porous network is released. The current

study begins with the investigation of different aluminum hydroxide/MO precursor mass ratios on the effect of specific surface area of iron oxide and cobalt oxide. It can be seen from the XRD pattern (**Figure S1A**) that all Fe_2O_3-Y-400 samples subject to calcination at 400 °C exhibit the characteristic diffractions attributed to Fe_2O_3 (PDF#33-0664),[31,32] and the crystallite size calculated by Scherrer's equation is about 13.5 nm. The structure and pore property of Fe_2O_3-Y-400 were analyzed by nitrogen sorption-desorption measurement performed at −196 °C, and the results are presented in **Figure S2**. It was noted that all Fe_2O_3-Y-400 displays type-IV curves with H3 hysteresis loops in the range of P/P_0 = ∼0.4−1.0, revealing their mesoporous structures. The pore size distributions obtained by the Barrett-Joyner-Halenda (BJH) model are narrow and centered at 2−4 nm, which are obviously smaller than the crystallite size of Fe_2O_3-Y-400, demonstrating their intracrystalline pores. In addition, note that the specific surface area (S_{BET}) of Fe_2O_3-Y-400 first increases and then decreases with the increasing of aluminum hydroxide/iron oxide precursor, and it reaches the largest when the mass ratio of aluminum hydroxide/iron oxide precursor is 1.0 (280 $m^2 \cdot g^{-1}$). It is well-known that higher calcination temperature is conductive to obtaining better crystallinity, but it also may result in the pore collapse.[33,34] The effect of calcination temperature on the property of Fe_2O_3-1-Z was further studied. As shown in **Figure 1A**, all Fe_2O_3-1-Z samples present the typical reflections assigned to Fe_2O_3 (PDF#33-0664), and the peak intensities grow stronger with the rising of calcination temperature. Additionally, it also can be seen that the calcination temperature exert distinct effect on the pore property of Fe_2O_3-1-Z (as shown in **Scheme 1**), and Fe_2O_3-1-400 possesses the largest S_{BET} value. Further elevating calcination temperature leads to the reduction of S_{BET}. In sharp contrast, the Fe_2O_3-Z samples prepared without aluminum hydroxide show distinctly lower S_{BET} value and broader pore size compared with Fe_2O_3-Y-Z (as illustrated in **Table 1** and **Figure S3**), in turn elucidating the crucial role of aluminum hydroxide as the structure-directing agent.

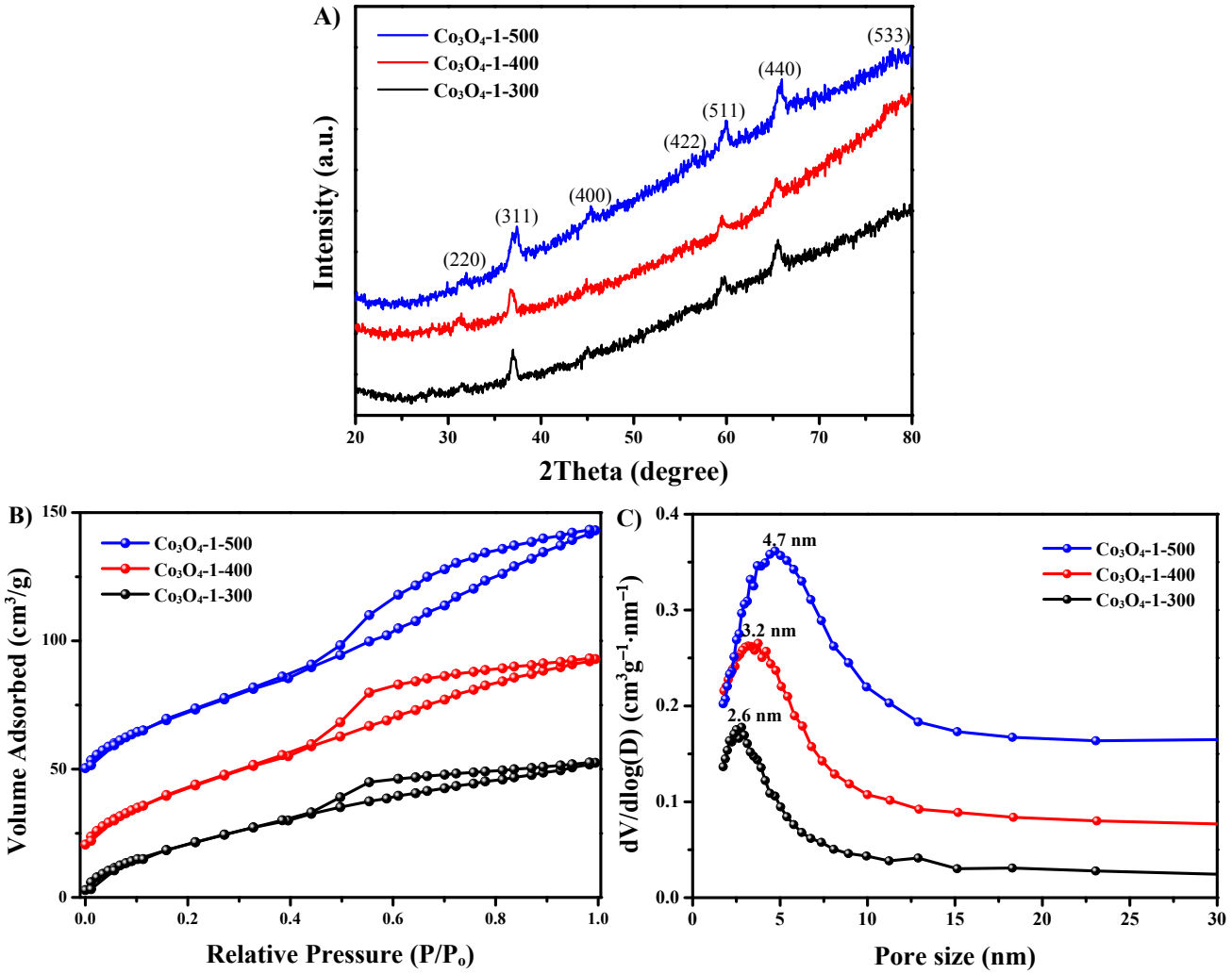

Figure 2. (A) XRD patterns, (B) N_2 adsorption-desorption isotherms (−196 °C), and the pore size distributions (C) of Co_3O_4 prepared by mechanochemical nanocasting at different calcination temperatures.

As an important support/catalyst in catalysis field, cobalt oxide has attracted considerable interest because of its unique physicochemical property.[35-40] Currently, we have also tried to synthesize cobalt oxide with mesoporous structure. **Figure 2A** reveals that all cobalt oxides show the characteristic diffraction peaks corresponding to crystalline Co_3O_4 phase (PDF#43-1003),[41,42] and the intensities of diffraction peaks gradually increase with the increasing of calcination temperature, revealing the crystallinity of Co_3O_4 increases. The crystal sizes of Co_3O_4 were estimated to be 10−14 nm by Scherrer's equation. The mesoporosity of Co_3O_4 was investigated by N_2 adsorption-desorption isotherms, which exhibits Type IV isotherms (**Figure 2B**) with H3-type hysteresis loops in the range of P/P_0 = 0.4−1.0, demonstrating their mesoporous structures. The pore size distributions by resolving the adsorption branches of the isotherm with BJH model are narrow

and centered at 2−5 nm (**Figure 2C**). And their S_{BET} value summarized in Table 1 shows that all Co_3O_4 samples prepared by aluminum hydroxide as a structure-directing agent give rise to much larger S_{BET} values and narrower pore sizes than those without aluminum hydroxide as template (as illustrated in **Table 1**, **Figure S4**, and **Figure S5**).

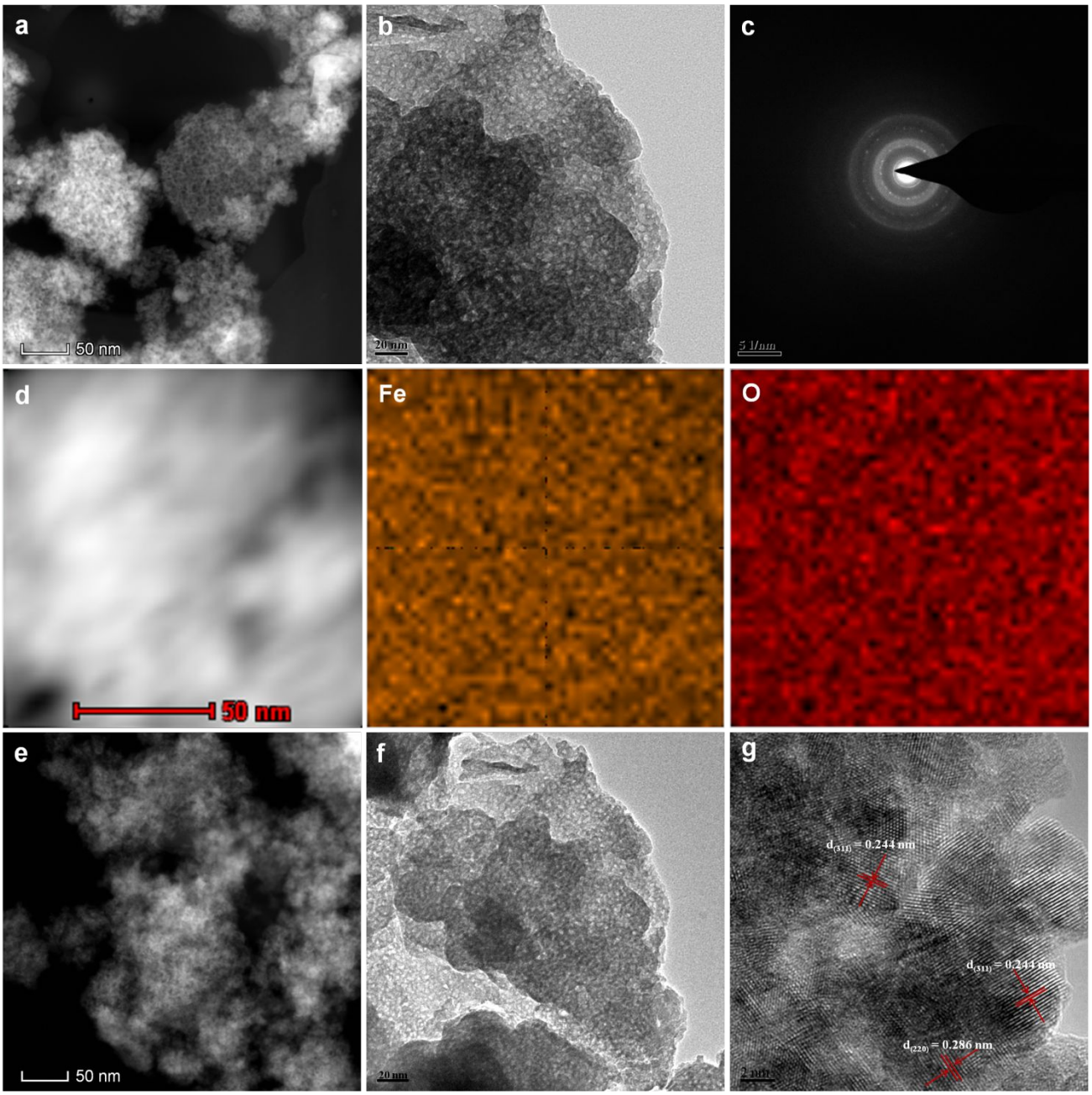

Figure 3. (a) STEM-HADDF image, scale bar 50 nm; (b) TEM image, scale bar 20 nm, (c) SAED pattern, and (d) EDS mapping images of elemental Fe and O for Fe_2O_3-1-400, scale bar 50 nm; (e) STEM-HADDF image, scale bar 50 nm; (f) TEM image, scale bar 20 nm and (g) HRTEM image of Co_3O_4-1-400, scale bar 2 nm.

The structural properties of the representative Fe_2O_3-1-400 and Co_3O_4-1-400 were elucidated by STEM-HAADF and HRTEM. As presented in **Figure 3a and b**, Fe_2O_3-1-400 shows a spongelike nanoarchitecture that composed of abundant mesopores with pore size ranging from 2 to 5 nm, which is consistent with the N_2 sorption-desorption results. The selected-area electron diffraction (SAED) pattern was performed to explore the overall composition of the as-prepared ferric oxide. The result was illustrated in **Figure 3c,** which elucidates the diffraction spots attributed to Fe_2O_3 crystalline phase.[43] EDS mapping images (**Figure 3d**) further verify the uniform distribution of Fe and O in Fe_2O_3-1-400. Meanwhile, STEM-HAADF image (**Figure 3e**) illustrates the porous structure of Co_3O_4, and TEM image (**Figure 3f**) shows that the nanoarchitecture consists of rich porosity with narrow pore sizes centered at around 3 nm. HRTEM was carried out to investigate the phase composition of Co_3O_4. It is noted that lattice fringes with distance of 0.244 and 0.286 nm can be found in HRTEM image (**Figure 3g**), which corresponds to d-spacing of (311) and (220) crystal planes of cobalt oxide,[44,45] respectively. It accords well with the XRD results.

In order to get insight into the formation process of mesoporous structure in the as-fabricated samples, we first performed the SEM for aluminium hydroxide (CAS: 21645-51-2), which exhibits irregular particles with sizes from 20 to ~100 nm (**Figure S6**). Actually, abundant mesopores in the range of ~2-8 nm were observed inside bulk particles. Subsequently, we collected the SEM images of Al_2O_3 formed by ball milling of the aluminium hydroxide in zirconia reactor for 1 h followed by calcinated at 400 °C in air for 3 h, which also shows ununiform particle size between 20 and 300 nm. Then, we further carried out EDS mapping for the precursors of Fe_2O_3-1-400 before the removal of Al (as shown in **Figure S5**). It confirms the presence and uniform distribution of Fe, Al, and O in the both the precursors of Fe_2O_3-1-400 and no mesopores are observed on the surface of the bulk materials. In stark contrast, the pore sizes of the as-prepared metal oxide samples via aluminum hydroxide-directing mechanochemical nanocasting strategy are located in the range of 3~6 nm, roughly in agreement with the pore of aluminium hydroxide. Therefore, it can be induced that the pores in these mesoporous metal oxides should be mainly induced by the removal of aluminium hydroxide. The mechanical force and friction heating may drive the mechanochemical mixing between the metal oxide precursors and aluminum hydroxide.

Based on the results mentioned above, we put forward an aluminum hydroxide-directing mechanochemical nanocasting for the synthesis of mesoporous Fe_2O_3 and Co_3O_4. This technology enables high degree of synthesis of these oxides with relative high specific surface area, abundant mesoporous structure, and narrow pore size. Thereafter, we extended the scope of aluminum hydroxide-directing mechanochemical nanocasting for the preparation of other mesoporous MOs. It is noteworthy that the CeO_2, ZrO_2, LaO_3, and CuO_x calcinated at 400 °C exhibit high S_{BET} of 192, 170, 103, and 74 $m^2 \cdot g^{-1}$, respectively. In addition, in order to demonstrate the advantage of this synthesis strategy compared with common hard-templating synthesis, we further employed a water-insoluble metal precursor cerium carbonate hydrate ($Ce_2(CO_3)_3 \cdot xH_2O$, CAS: 54451-25-1) as metal precursor for the synthesis of mesoporous CeO_2. As shown in **Table 1**, the as-synthesized CeO_2 shows S_{BET} of 177 $m^2 \cdot g^{-1}$, which is almost comparable with that of $Ce(NO_3)_3 \cdot 6H_2O$ as precursor.

Table 1. Structural properties of mesoporous MOs.

Sample	S_{BET}($m^2 \cdot g^{-1}$)	Pore volume ($cm^3 \cdot g^{-1}$)	Average pore size (nm)
Al_2O_3-400	49	0.29	26.5
Bulk-Fe_2O_3-400	8.1	0.01	–
Fe_2O_3-0.5-400	172	0.16	3.7
Fe_2O_3-1-400	280	0.57	5.4
Fe_2O_3-2-400	204	0.14	3.1
Fe_2O_3-1-300	225	0.14	2.8
Fe_2O_3-1-500	251	0.18	3.4
Fe_2O_3-300	79.3	0.12	12.9
Fe_2O_3-400	43.9	0.12	6.6
Fe_2O_3-500	14.0	0.12	30
Bulk-Co_3O_4	6.0	0.01	–
Co_3O_4-1-300	139	0.11	3.8
Co_3O_4-1-400	155	0.14	3.8
Co_3O_4-1-500	142	0.16	4.8
Co_3O_4-300	65.4	0.41	16.3
Co_3O_4-400	39.8	0.41	20.8
Co_3O_4-500	17.5	0.17	13.4
CeO_2-1-400	192	0.21	5.7
CeO_2-1-400$_{(Ce2(CO3)3 \cdot xH2O)}$	177	0.30	6.9
ZrO_2-1-400	170	0.18	6.2
LaO_3-1-400	103	0.39	16.4

CuO_x-1-400	74	0.10	18.0
CuO_x-CeO_y-1-400	177	0.30	4.1
FeO_x-CeO_y-1-400	170	0.16	3.9
CoO_x-CuO_y-CeO_z-1-400	154	0.26	5.4
CoO_x-FeO_y-CeO_z-1-400	133	0.20	6.2

Multi-component MOs generally show better catalytic activity than the corresponding single component MO counterparts because of their unique synergetic effects.[46-49] The catalytic oxidation of carbon monoxide (CO) is a widely used probe reaction to investigate oxidation catalysts. Therefore, we tried to further extend the mechanochemical nanocasting to synthesize mesoporous CuO_x-CeO_y, FeO_x-CeO_y, CoO_x-CuO_y-CeO_z, and CoO_x-FeO_y-CeO_z complexes for CO oxidation. The both XRD patterns (**Figure 4A**) of CuO_x-CeO_y-1-400, FeO_x-CeO_y-1-400, CoO_x-CuO_y-CeO_z-1-400, and CoO_x-FeO_y-CeO_z-1-400 calcinated at 400 °C show distinct diffraction peaks assigned to CeO_2, and no other reflections corresponding to Cu or/and Fe or/and Co crystalline species were detected. It indicates that Cu, Fe, and Co species are highly dispersed within ceria. The contents of Al, Cu, Fe, Co determined by ICP-AES were 0.04%, 10.2%, 33.7%, 12.5%, respectively. Then, the porosity of CuO_x-CeO_y-1-400, FeO_x-CeO_y-1-400, CoO_x-CuO_y-CeO_z-1-400, and CoO_x-FeO_y-CeO_z-1-400 complexes were examined by N_2 adsorption-desorption measurements, and the results are displayed in **Figure 4B and C**. It can be observed that the both samples exhibit type-IV isotherms with H3-type hysteresis loops, typical features of mesoporous materials. Their S_{BET} values are 177, 170, 154, and 133 $m^2 \cdot g^{-1}$ (as presented in Table 1), respectively, which are slightly lower than that of pristine CeO_2. It furthers demonstrates the homogenous distribution of Cu, Fe, and Co species within ceria. The porous morphology and phase composition of the representative FeO_x-CeO_y-1-400 and CoO_x-FeO_y-CeO_z-1-400 complexes were further analyzed by STEM-HAADF and HRTEM (**Figure 5**). Both the **Figure 5a and 5d** show sponge-like nanoarchitecture with rich pores in the samples. HRTEM images illustrate that clear lattice fringes were recognized for crystalline Co_3O_4, Fe_2O_3, and CeO_2 in different domains (**Figure 5b and 5e**).[45,43,50] EDS mapping images (**Figure 5c and 5f**) further testify the uniform distribution of Co, Fe, Ce, and O in FeO_x-CeO_y-1-400 and CoO_x-FeO_y-CeO_z-1-400 complexes.

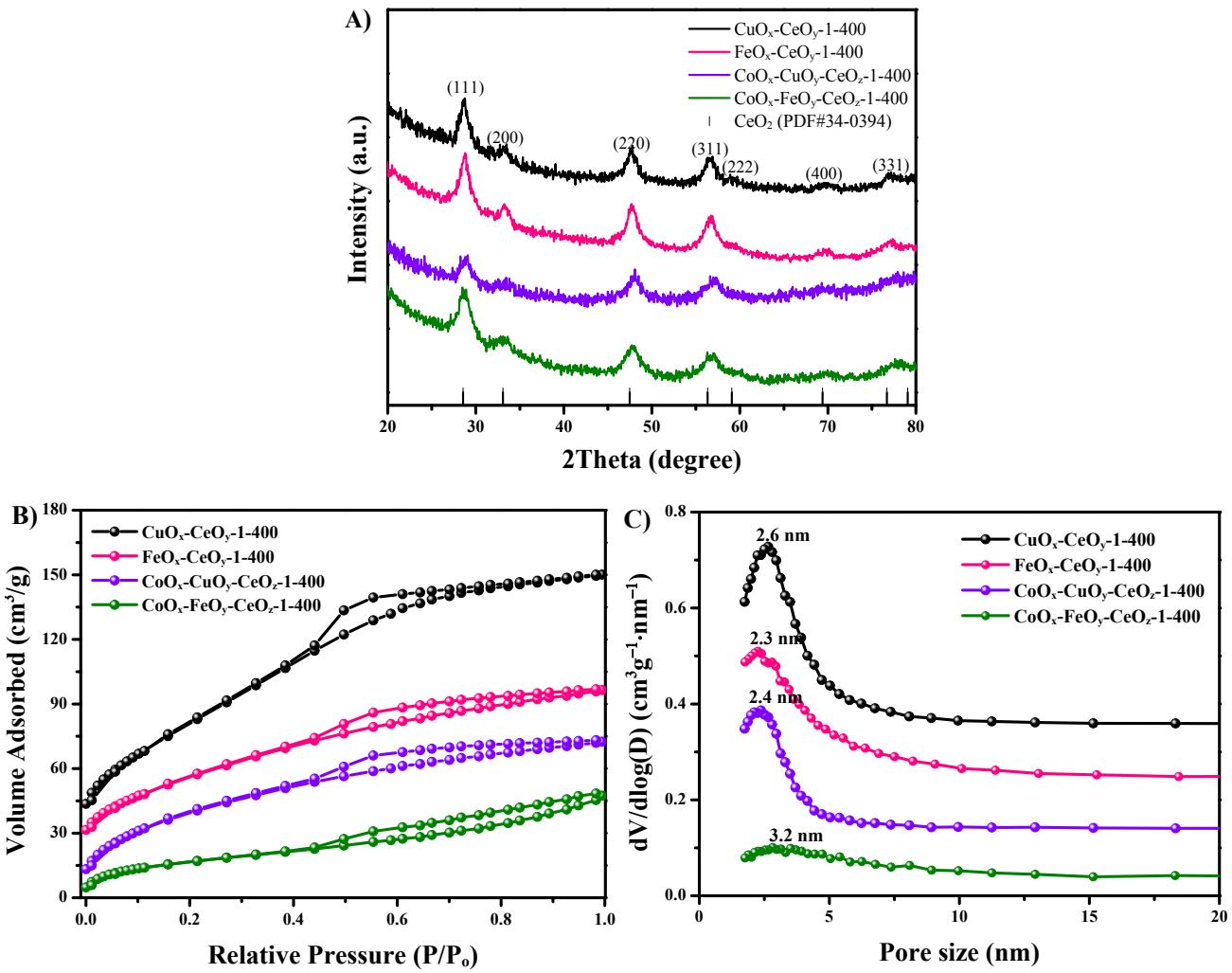

Figure 4. (A) XRD patterns, (B) N_2 adsorption-desorption isotherms (−196 °C), and (C) the pore size distributions of CuO_x-CeO_y-1-400, FeO_x-CeO_y-1-400, CoO_x-CuO_y-CeO_z-1-400, and CoO_x-FeO_y-CeO_z-1-400 prepared by mechanochemical nanocasting at 400 °C.

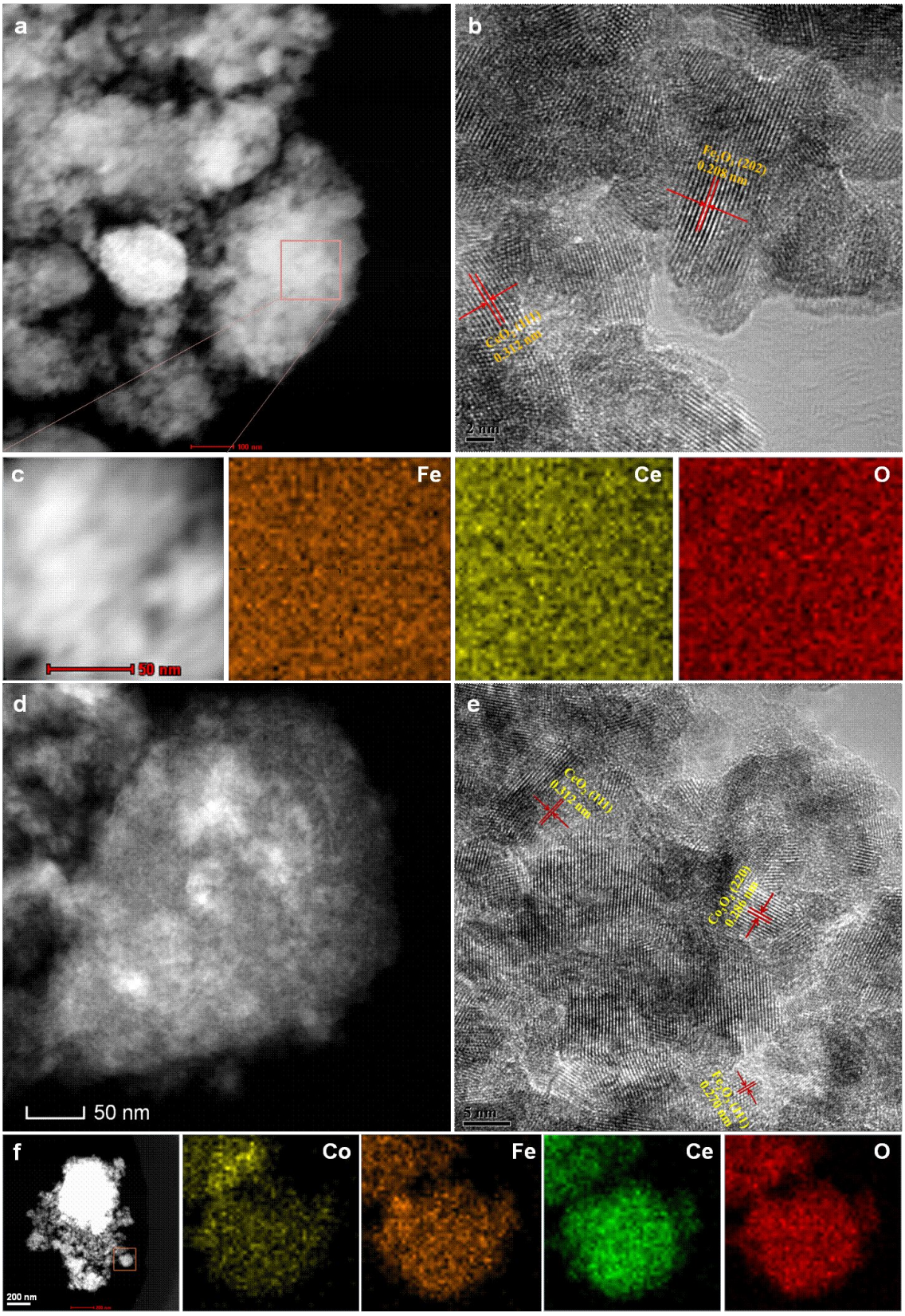

Figure 5. (a) STEM-HADDF image, scale bar 100 nm; (b) HRTEM image, scale bar 2 nm; and (c) EDS mapping images of elemental Fe, Ce, and O for FeO_x-CeO_y-1-400, scale bar 50 nm; (d) STEM-HADDF image, scale bar 50 nm (e) HRTEM image, scale bar 5 nm; and (f) EDS mapping images of elemental Co, Fe, Ce, and O for CoO_x-FeO_y-CeO_z-1-400, scale bar 200 nm.

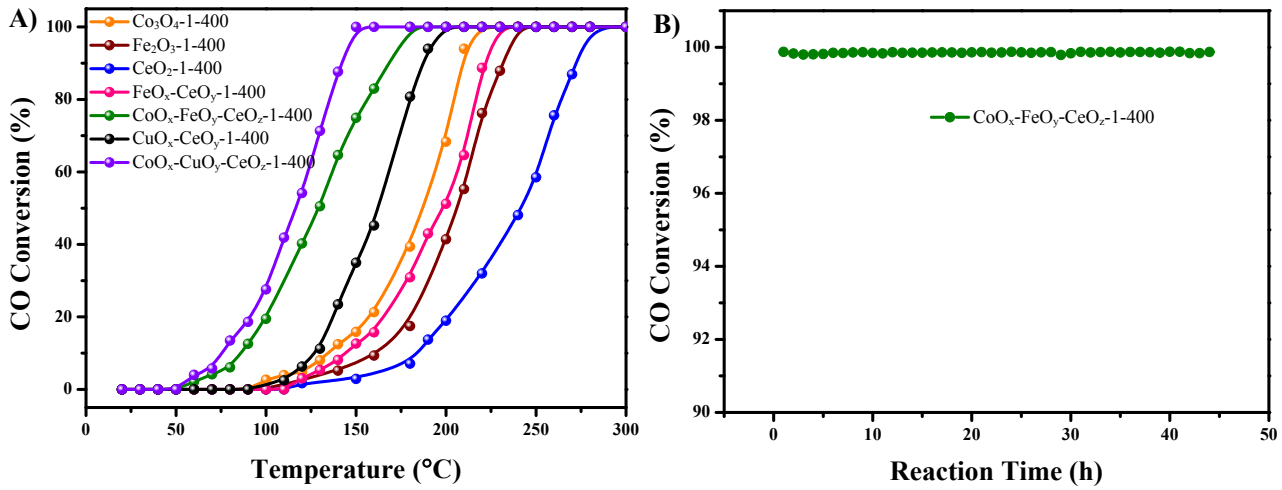

Figure 6. (A) CO conversion as a function of temperature over Co_3O_4-1-400, Fe_2O_3-1-400, CeO_2-1-400, CuO_x-CeO_y-400, FeO_x-CeO_y-400, CoO_x-CuO_y-CeO_z-400, and CoO_x-FeO_y-CeO_z-1-400; (B) CO conversion as a function of time over the representative CoO_x-FeO_y-CeO_z-1-400 upon reaction at a temperature of 400 °C.

Mesoporous metal oxides have been widely employed in heterogeneous catalysts and have shown impressive catalytic activity. An and Ren fabricated a series of ordered mesoporous metal oxides, such as Co_3O_4 (~90 m^2/g), Fe_2O_3 (~130 m^2/g), CeO_2 (~152 m^2/g), using mesoporous silica KIT-6 as the hard template to be used for CO oxidation,[51,52] which show completely CO conversion at 130, 300, and 360 °C, respectively. In this study, the catalytic activities of these as-synthesized porous Co_3O_4-1-400, Fe_2O_3-1-400, CeO_2-1-400, CuO_x-CeO_y-400, FeO_x-CeO_y-400, CoO_x-CuO_y-CeO_z-400, and CeO_x-FeO_y-CeO_z-1-400 complexes were also examined for CO oxidation. As shown in **Figure 6**, Co_3O_4-1-400, Fe_2O_3-1-400, and CeO_2-1-400 obtain 100% CO conversion at 220, 245, 290 °C, which are clearly lower than the corresponding oxides prepared by the hard template. It demonstrates the advantage of aluminium hydroxide-directing mechanochemical nanocasting strategy introduced in this work. In addition, the FeO_x-CeO_y-1-400 and CoO_x-FeO_y-CeO_z-1-400 achieved completely CO conversion at 230 and 180 °C, respectively, which are notably lower than either monometal oxide counterpart because of the enhanced redox abilities that should be conductive to CO oxidation (**Figure S8**). In addition, compared with FeO_x-CeO_y-400 and CoO_x-FeO_y-CeO_z-1-400 counterparts, the corresponding Cu-based complexes exhibited distinctly higher activities, which demonstrated 200 and 150 °C for 100% CO conversion. Furthermore, we studied the thermal stability of the representative CoO_x-FeO_y-CeO_z-1-400 catalyst

for CO oxidation. It still kept 100% CO conversion for 44 h. Therefore, they have promising potential in the elimination of CO in practical application.

4. Conclusions

In summary, we demonstrate a low-cost and facile aluminium hydroxide-directing mechanochemical nanocasting strategy to successfully synthesize a series of mesoporous MOs and complexes, which exhibit high specific surface area and excellent catalytic performance for CO oxidation. Moreover, the presented strategy enables a facile and rapid synthesis oxide in a short time, which overcomes the defects associated with the traditional wet process. It is expected that this technology may open up new opportunities for fabricating a number of advanced porous materials with high surface area and narrow pore size in the near future.

Acknowledgements

ML, YL, ZZ, RT, and S.D. were supported by the Division of Chemical Sciences, Geosciences, and Biosciences, Office of Basic Energy Sciences, US Department of Energy. J.X.L. and J.L. thank the National Natural Science Foundation of China (21673290, U1662103). P.F.Z. and J. F. B. acknowledge Thousand Talent Program, National Natural Science Foundation of China (Grant No. 21776174), the Open Foundation of the State Key Laboratory of Ocean Engineering (Shanghai Jiao Tong University of China) (No. 1809), and China Shipbuilding Industry Corporation for the support.

Conflict of Interest

The authors declare no conflict of interest.

References

1. Y. Zhao, F. Wang, C. Wang, S. Wang, C. Wang, Z. Zhao, L. Duan, Y. Liu, Y. Wu, W. Li and D. Zhao, *Nano Energy* 2019, 56, 426−433.

2. Y. Ma, Y. Zhang, X. Wang, M. Fan, K. Li, T. Wang, Y. Liu, Q. Huo, Z.-A. Qiao and S. Dai,

Nanoscale 2018, 10, 5731−5737.

3. C. Jo, J. Hwang, W.-G. Lim, J. Lim, K. Hur and J. Lee, *Adv. Mater.* 2018, *30*, 1703829.
4. G. Feng, J. Wang, M. Boronat, Y. Li, J.-H. Su, J. Huang, Y. Ma and J. Yu, *J. Am. Chem. Soc.* 2018, 140, 4770−4773.
5. X.-Y. Yang, L.-H. Chen, Y. Li, J. C. Rooke, C. Sanchez and B.-L. Su, *Chem. Soc. Rev.* 2017, 46, 481−558.
6. P. Zhang, H. Lu, Y. Zhou, L. Zhang, Z. Wu, S. Yang, H. Shi, Q. Zhu, Y. Chen and S. Dai, *Nat. Commun.* 2015, 6, 8446.
7. A. S. Poyraz, C.-H. Kuo, S. Biswas, C. K. King'ondu and S. L. Suib, *Nat. Commun.* 2013, 4, 2952.
8. Y. Ren, Z. Ma and P. G. Bruce, *Chem. Soc. Rev.* 2012, 41, 4909−4927.
9. J. Liu and D. Xue, *Adv. Mater.* 2008, 20, 2622−2627;
10. T. Y. Ma, S. Dai, M. Jaroniec and S. Z. Qiao, *J. Am. Chem. Soc.* 2014, 136, 13925−13931;
11. G. Wang, J. Qin, X. Zhou, Y. Deng, H. Wang, Y. Zhao and J. Wei, *Adv. Funct. Mater.* 2018, 28, 1806144.
12. H. Wang, S. Zhuo, Y. Liang, X. Han and B. Zhang, *Angew. Chem. Int. Edit.* 2016, 55, 9055−9059.
13. A. Feinle, M. S. Elsaesser and N. Huesing, *Chem. Soc. Rev.* 2016, 45, 3377−3399.
14. J. Lee, M. C. Orilall, S. C. Warren, M. Kamperman, F. J. Disalvo and U. Wiesner, *Nat. Mater.* 2008, 7, 222−228.
15. H. F. Yang and D. Y. Zhao, *J. Mater. Chem.* 2005, 15, 1217−1231.
16. F. Schuth, *Angew. Chem. Int. Edit.* 2003, 42, 3604−3622.
17. P. F. Fulvio, S. S. Brown, J. Adcock, R. T. Mayes, B. K. Guo, X. G. Sun, S. M. Mahurin, G. M. Veith and S. Dai, *Chem. Mater.* 2011, 23, 4420−4427.
18. S. K. Han, C. Gu, M. Gong and S. H. Yu, *J. Am. Chem. Soc.* 2015, 137, 5390−5396.
19. X.W. Lou, D. Deng, J. Y. Lee, J. Feng and L. A. Archer, *Adv. Mater.* 2008, 20, 258−262.
20. H. B. Wu, B. Y. Xia, L. Yu, X. Y. Yu and X.W. Lou, *Nat. Commun.* 2015, 6, 6512.
21. P. D. Yang, D. Y. Zhao, D. I. Margolese, B. F. Chmelka and G. D. Stucky, *Chem. Mater.* 1999, 11, 2813−2826.

22. G. J. D. Soler-illia, C. Sanchez, B. Lebeau and J. Patarin, *Chem. Rev.* 2002, 102, 4093−4138.

23. Y. Deng, J. Wei, Z. Sun and D. Zhao, *Chem. Soc. Rev.* 2013, 42, 4054−4070.

24. J. Wei, Z. Sun, W. Luo, Y. Li, A. A. Elzatahry, A. M. Al-Enizi and D. Zhao, *J. Am. Chem. Soc.* 2017, 139, 1706−1713.

25. W. Xiao, S. Yang, P. Zhang, P. Li, P. Wu, M. Li, N. Chen, K. Jie, C. Huang, N. Zhang and S. Dai, *Chem. Mater.* 2018, 30, 2924−2929.

26. W. Yue and W. Zhou, *Prog. Nat. Sci-Mater.* 2008, 18, 1329−1338.

27. M. Zhang, L. He, T. Shi and R. Zha, *Chem. Mater.* 2018, 30, 7391−7412.

28. X. Deng, K. Chen and H. Tueysuez, *Chem. Mater.* 2017, 29, 40−52.

29. J. H. Smatt, F. M. Sayler, A. J. Grano and M. G. Bakker, *Adv. Eng. Mater.* 2012, 14, 1059−1073.

30. X. Sun, Y. Shi, P. Zhang, C. Zheng, X. Zheng, F. Zhang, Y. Zhang, N. Guan, D. Zhao and G. D. Stucky, *J. Am. Chem. Soc.* 2011, 133, 14542−14545.

31. M. H. Oh, T. Yu, S. H. Yu, B. Lim, K. T. Ko, M.-G. Willinger, D. H. Seo, B. H. Kim, M. G. Cho, J. H. Park, K. Kang, Y. E. Sung, N. Pinna and T. Hyeon, *Science* 2013, 340, 964−968.

32. K. E. deKrafft, C. Wang and W. Lin, *Adv. Mater.* 2012, 24, 2014−2018.

33. D. Chen, J. Zhao, P. F. Zhang and S. Dai, *Polyhedron* 2019, 162, 59–64.

34. J. Zhao, Y. Shu and P. F. Zhang, *Chinese J. Catal.* 2019, 40, 1078–1084.

35. L. Wang, J. Wan, Y. Zhao, N. Yang and D. Wang, *J. Am. Chem. Soc.* 2019, 141, 2238−2241.

36. H. C. Li, Y. J. Zhang, X. Hu, W. J. Liu, J. J. Chen and H. Q. Yu, *Adv. Eng. Mater.* 2018, 8, 1702734.

37. H. H. Pham, M. J. Cheng, H. Frei and L. W. Wang, *ACS Catal.* 2016, 6, 5610−5617.

38. R. Black, J. H. Lee, B. Adams, C. A. Mims and L. F. Nazar, *Angew. Chem. Int. Edit.* 2013, 52, 392−396.

39. H. F. Wang, R. Kavanagh, Y. L. Guo, Y. Guo, G. Z. Lu and P. Hu, *Angew. Chem. Int. Edit.* 2012, 51, 6657−6661.

40. C. Y. Ma, Z. Mu, J. J. Li, Y. G. Jin, J. Cheng, G. Q. Lu, Z. P. Hao and S. Z. Qiao, *J. Am. Chem. Soc.* 2010, 132, 2608−2613.

41. P. Ge, C. Zhang, H. Hou, B. Wu, L. Zhou, S. Li, T. Wu, J. Hu, L. Mai and X. Ji, *Nano Energy*

2018, *48*, 617−629.

42. S. Bala, I. Mondal, A. Goswami, U. Pal and R. Mondal, *J. Mater Chem. A* 2015, 3, 20288−20296.
43. O. Lupan, V. Postica, N. Wolff, O. Polonskyi, V. Duppel, V. Kaidas, E. Lazari, N. Ababii, F. Faupel, L. Kienle and R. Adelung, *Small* 2017, 13, 1602868.
44. A. Cazacu, C. Larosa, P. Beaunier, G. Laurent, P. Nanni, L. Mitoseriu and I. Lisiecki., *Adv. Funct. Mater.* 2014, 24, 164−170.
45. I. Lopes, N. El Hassan, H. Guerba, G. Wallez and A. Davidson, *Chem. Mater.* 2006, *18*, 5826−5828.
46. A. Yu, C. Lee, N. S. Lee, M. H. Kim and Y. Lee, *ACS Appl. Mater. Inter.* 2016, 8, 32833−32841.
47. J. Graciani, K. Mudiyanselage, F. Xu, A. E. Baber, J. Evans, S. D. Senanayake, D. J. Stacchiola, P. Liu, J. Hrbek, J. Fernandez Sanz and J. A. Rodriguez, *Science* 2014, 345, 546−550.
48. C. Yuan, H. B. Wu, Y. Xie and X. W. Lou, *Angew. Chem. Int. Edit.* 2014, 53, 1488−1504.
49. J. B. Park, J. Graciani, J. Evans, D. Stacchiola, S. D. Senanayake, L. Barrio, P. Liu, J. F. Sanz, J. Hrbek and J. A. Rodriguez, *J. Am. Chem. Soc.* 2010, 132, 356−363.
50. Q. Li, W. Xie, G. Chen, Y. Li, Y. Huang and X. Chen, *Nano Res.* 2015, 8, 3075−3084.
51. K. An, S. Alayoglu, N. Musselwhite, S. Plamthottam, G. Melaet, A. E. Lindeman and G. A. Somorjai, *J. Am. Chem. Soc.* 2013, 135, 16689−16696.
52. Y. Ren, Z. Ma, L. Qian, S. Dai, H. He and P. G. Bruce, *Catal. Let.* 2009, 131, 146−154.

Table of Contents Entry

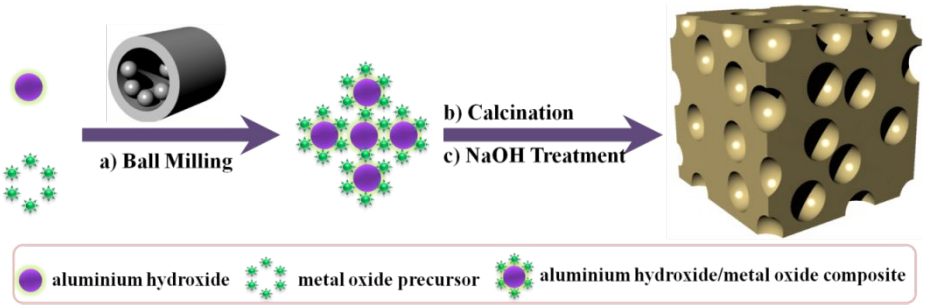

Mechanochemical nanocasting strategy featured by aluminum hydroxide as the mesoporous structure-directing agent to fabricate mesoporous metal oxides